Article

Spatiotemporal heterogeneity of green land and its effect on the thermal comfort of urban human settlements in the central coast of China, a case in Rizhao region

Tao Pan[1,2], Shanfeng He[1,] *, Zhaoyu Liu[3], Liming Jiang[1], Qinglei Zhao[1] and Rafiq Hamdi[4,5]

[1] School of Geography and Tourism, Qufu Normal University, Shandong, Rizhao, 276826, China, pantao@qfnu.edu.cn; qlzhao0119@qfnu.edu.cn; lyjiangliming@163.com;
[2] Key Laboratory of Land Surface Pattern and Simulation, Institute of Geographic Sciences and Natural Resources Research, Chinese Academy of Sciences, Beijing 100101, China;
[3] School of Computer Science, Qufu Normal University, Shandong, Rizhao, 276826, zhyliu@qfnu.edu.cn;
[4] Royal Meteorological Institute, 1180 Brussels, Belgium, rafiq.hamdi@meteo.be;
[5] Department of Physics and Astronomy, Ghent University, 9000 Ghent, Belgium.
* Correspondence: e-mail: hesf2020@qfnu.edu.cn; Tel.: +86-19862356365

Abstract: The central coast is one of the importantly livable regions in China, and green land plays a meaningful role in improving human settlements through regulating ecosystem services. However, the research on spatiotemporal heterogeneity of green land in different urbanized areas are still lacking in this region, which limits the timeliness of reporting on the land-surface thermal properties of residential environment from green land perspective. To address this issue, the synergistic methodology of "artificial numerical technology -- urban interior mixed pixel classification -- surface radiation energy balance model" was applied to investigate the green land change and its impact on human settlements in Rizhao region, which is known for its coastal ecology and greenery in China and obtained the United Nations habitat award. Main conclusions of this study are below: (1) Although total green land decreased by 474.05 km^2, resulting in a decrease of 9.17% in its share of the entire study area from 2000-2022 during the urbanization process, but the greening levels improved within the built-up area, with the greening proportion of 25.34% in 2000 and 42.98 km^2 in 2022. (2) Differences in green land at different urbanized regions were first observed, namely, urban greening rate was 37.78% in the old urban areas of 2022, while it was up to 46.43% in new urban areas. More attention was paid to the construction of urban green space during urban expansion, which will inevitably bring better visual and comfort experience to residents. (3) Thermal comfort indicators for urban residents were evaluated in latent heat flux (0-457.83 W/m^2), sensible heat flux (0-645.09 W/m^2), total available energy (254.07-659.42 W/m^2) and others. (4) The lowered cooling temperature effect in the middle, high green land density region was 1.05 ℃ and 2.12 ℃ compared to the low-density region, and the average air temperature was 25.86 ℃. Also, spatial patterns of hot and cold uncomfortable areas were displayed in this study. Overall, this study provides the meaningfully practical reference for exploring the spatiotemporal heterogeneity of green land and its impact on residents' environments from the perspective of land-surface thermal properties in coastal areas of China and around the world.

Keywords: Land use; greening; land-surface thermal properties; residential environments; central coast region of China.

1. Introduction

In hot summer, people are often attracted to the cool climate of coastal cities [1]. However, with the continuous deepening of the urbanization process [2], the reinforced concrete buildings may bring the agglomeration effect of urban heat waves and form the thermal discomfort region for residents in the coastal urban areas [3-5]. The reasonable layout of green land space can usually cope with extreme summer temperatures and avoid the discomfort for local residents or tourists such as heatstroke, thereby improving the ecosystem service function [6,7]. China is still undergoing a rapid urbanization process, shifting from a single urban expansion in the past to a more emphasis on a rational urban planning and layout, along with the harmonious coexistence between people and nature [8,9]. In the context of current urban construction of sponge cities, livable cities, innovative cities, and ecological cities in China, green land space plays the

 doi:10.20944/preprints202304.0424.v1

more and more important role in this process [10]. Especially in face of the future desire of carbon peak in 2030 and carbon neutrality in 2060, the city's carbon digestion capacity further requires the improvement of the green land distribution pattern [11-13]. The study on spatiotemporal heterogeneity of green land space and its impact on residents' comfort from the perspective of land-surface thermal properties continues to become a hot topic worldwide.

For the display of spatiotemporal heterogeneity of green land, scholars continue to investigate all the time [14,15]. Early green land space survey mainly relied on manpower and measuring equipment for measurement, which was time-consuming and inefficient [16]. With the development of remote sensing earth observation technology, new satellite sensors can be used to obtain information about the earth's surface such as green land [17,18]. The imaging resolution of ground objects has continuously increased from 1000 to 300 m, 30 m, 10 m, or even sub-meters. In the context of current big data and cloud platforms, green space monitoring is becoming more active [19]. Many green space mapping products emerge spontaneously using the remote sensing satellite such as Global 30 m land mapping products released by the National Bureau of Surveying and Mapping and the global 10 m resolution global land cover mapping for 2017 prepared by the Tsinghua University team [20]. Among these products, the vector land product released by the Chinese Academy of Sciences from 1980s to 2020 has multi period data, 25 land classification types and has achieved good scientific research results in China's global, regional and local investigations. The vector data also has the advantage of high accuracy [21-23]. Considering the timeliness of multiple periods and the diversity of land classification, it was used in the monitoring research of green land space in this study as the land background carrier.

Research on the comfort of human settlements from land-surface thermal properties, early, it mainly focused on the evaluation of the thermal environment of buildings on the workers [24]. Subsequently, Universal Thermal Climate Index (i.e., UTCI) was proposed to focus the relationship between human settlements and factors of land surface convection, thermal radiation, water evaporation, and artificial respiration [25,26]. Additionally, the impact of green land space on the comfort of human settlements was continuously explored, considering that vegetation naturally had a physical shielding property, which affected air flow and heat exchange within the environment through horizontal blocking effects, resulting in a decrease in ambient temperature; and it further intercepted solar radiation through vertical shading, creating relatively low temperature areas under vegetation in the form of shadows [26,27]. Scholars conducted in-depth research on the comfort of living environment from greening land perspective using temperature and humidity index, comfort index, and wind efficiency index in the regions of urban green land space and parks, thereby optimizing the layout of green land space and parks to improve the living environment [28,29]. The popularization of remote sensing technology has led these studies to move from statistics to space, and the spatial pattern is constantly improving such as the spatialized land-surface thermal property maps of land surface temperature, air temperature, net radiation, Bowen ratio, latent heat flux, available flux, and sensible heat flux [30-33].

The coastal areas of central China, with their suitable climate and environment, often attract tourists from all over the country. Currently, the report of green land space is insufficient, especially, research on green land space at different urbanization levels is still lacking, which led to the inability to report in a timely manner to explore the impact of green space on the comfort of human settlements in this region. Rizhao region is located in the central coastal area of China. Since 2000, the process of urbanization has been accelerating. In 2009, Rizhao region won the "the United Nations Habitat Award" for its outstanding achievements in "improving housing and infrastructure, and building a green home", which was the only region in China to receive this honor that year. Subsequently, Rizhao entered a faster stage of urbanization development and obtained more Chinese honors such as the “greening region”. However, the current depiction of the spatiotemporal heterogeneity of green space in this area is not sufficient, which restricts the exploration of the land-surface thermal property comfort of green land space for human settlements in the central coastal region of China. Thus, the purpose of this study is below: (1) To provide the timely reporting on the spatiotemporal heterogeneity of green land space and capture its new changing laws in the whole study area; (2) To further first assess the greening level at different stages of urban development and give the specific quantitative values; (3) To analysis of the impact of green land density and its thermal comfort factors on the residential environment; And (4) To characterize the cooling temperature effect of different green land regions and analysis of spatial distribution characteristics of cold and hot uncomfortable areas for urban dwellers. Then, we discussed Rizhao was a highly greening and livable region in the central coast of China, and further compared the differentiated green land structures in different climatic regions at home and abroad, and the possibly positive effects of densely green land space on the comfort of human welfare. The research results provide a new reference for the discussion of the green land pattern and the impact on the land-surface thermal property maps comfort of human settlements in coastal areas of China and around the world.

Preprints (www.preprints.org) | NOT PEER-REVIEWED | Posted: 17 April 2023 doi:10.20944/preprints202304.0424.v1

2. Method

2.1 Study area

Rizhao region is located between 118 ° 25 ′~119 ° 39 ′ E and 35 ° 04 ′~36 ° 04 ′ N, in the central coastal area of Chinese Mainland and southeast of Shandong Peninsula. Rizhao has a beautiful coast in China contained more 30 administrative sub-regions (Figure1 b). It has a temperate monsoon climate with a small temperature difference in four seasons, so the temperature in summer and winter is moderate, along with abundant water resources. The terrain exhibits a high numerical value in the middle and a flat surrounding area (Figure1 a).

Rizhao is a coastal ecological, livable, tourism, modern port region and portside industrial base in China. The length from north to south is about 82 kilometers, and the width from east to west is about 90 kilometers. Rizhao is known as the "Capital of Water Sports" and "Oriental Sun City". Rizhao won the United Nations Habitat Award for excellent environment. Also, Rizhao was awarded the titles of National Civilized City, National Forest City, National Environmental Protection Key City, and National Ecological Demonstration Zone Construction Pilot City, etc. Suitable ecology, livable environment, high coverage of green land and other factors, which makes Rizhao as a typical area for exploring the temporal and spatial change of green land and its impact on residents in China.

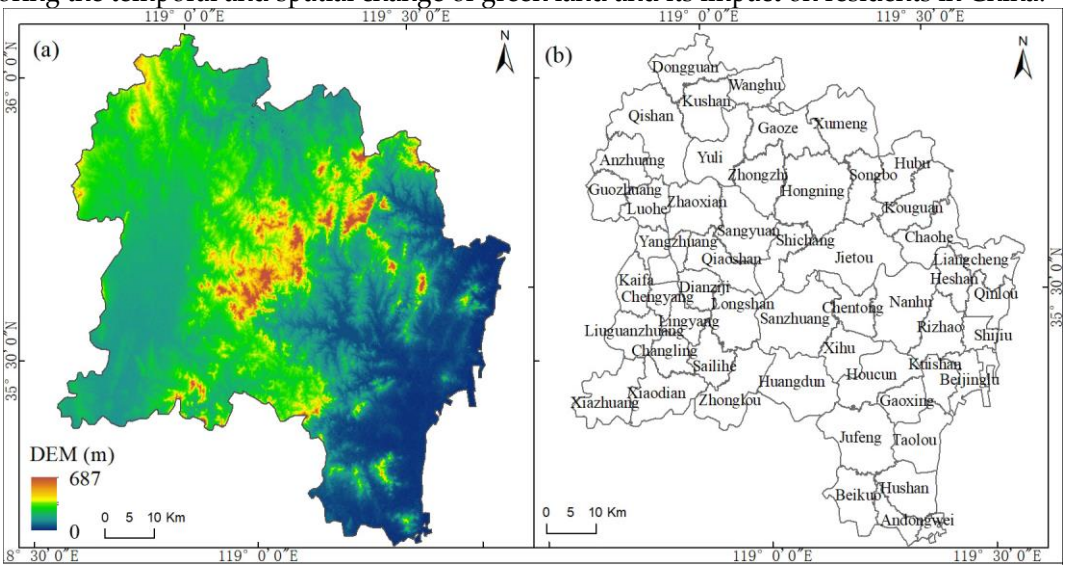

Figure 1 Overview map of the research area. (a) and (b) represented the spatial distribution of digital elevation model (DEM) and the administrative divisions, respectively.

2.2 Acquisition and processing of land use

2.2.1 Collection of land use data

Spatial land use maps of 2000, 2005, and 2010 in this study were from the Chinese Academy of Sciences, and its format of the data was vector that can provide accurate data statistics results. According to the land use classification system, the first level land types included 6 categories, and the second level types included 25 categories. Rich land classification systems can better describe the current situation of land use and its monitoring. In this study, the first level land types were classified as green land space system, including the cultivated land, forest land, grassland, and the non-green land space types, including the water body, construction land, and unused land. Then, the corresponding second level types of each first type were also automatically divided into green land space and non-green space, such as the green land space of upland crops, paddy field, woodland, shrub land, sparse forest land, other forest land, high coverage grassland, medium coverage grassland, and low coverage grassland.

2.2.2 Preprocessing land spatial map using the artificially digitized approach

Based on the 2010 land spatial classification map as the basic data source, we obtained the corresponding map for 2016 and 2022 here. United States Geological Survey (i.e., USGS) provided the free, universal, and better spectral characteristics of land resource satellites, which was also the main data source for the land use data production process of the Chinese Academy of Sciences. To maintain the consistency between the image data source and the Chinese Academy

Preprints (www.preprints.org) | NOT PEER-REVIEWED | Posted: 17 April 2023 doi:10.20944/preprints202304.0424.v1

of Sciences' land data, we used the remote sense of satellite from USGS for artificial visualization to obtain a land use map for 2016 and 2022. On the official website of USGS, the Landsat images with the features of poor quality, bad pixels, and cloud cover were filtered. Then, the images with available observation and high-quality were downloaded in the year of 2016 and 2022, which was used to generate green land maps for 2016 and 2022, respectively.

We performed false color band synthesis on Landsat images and used these images as the underlying layer on a professional software platform. The land spatial map of 2010 was superimposed on the corresponding images of 2016. In the land map 2010, a 2016 attribute table field was added, which was used to obtain the land cover types in 2016. Then, specialized manual identification of land use types was implemented using the professional knowledge by identifying the color, texture, and other characteristics of different land features on remote sensing images. The finally identified land type results were placed in the 2016 field of the attribute table 2010. After identifying the entire research area, a 2016 land spatial map was generated from 2016 field. To ensure the accuracy of 2016 data, the land use dynamic patches during 2010-2016 were obtained through the calculation of 2010 and 2016 fields. Different remote sensing professionals conducted multiple reviews of these dynamic patches, and the layered random verification scheme was also used to verify the accuracy and reliability of data. Finally, a spatial map of land use was generated in 2016 and the green land space data was extracted. Similarly, the 2022 green land map was also obtained in the same way.

2.3 Generation of green land density

The density data of green space can comprehensively analyze the pattern of green component, providing the basis impact of human settlements. For the analysis of green land density, ndvi index was widely used [34]. But when considering the different densities and classifications of urban areas, such as impermeable surface area, vegetation, water, and bare soil, ndvi may appear very simple, but it is still an important reference that has been added to this study for vegetation classification. To obtain different land types of density maps for comprehensive analysis, the linear spectral decomposition technology was adopted. The satellite images were first subjected to radiometric calibration processing to convert the brightness value of an image to absolute radiant brightness [35]. Image band fusion technology was used to upgrade the resolution of images from 30 m to 15 m, so that the land terrain pattern can be clearly depicted. Atmospheric correction conducted the process of eliminating the radiation errors caused by atmospheric effects and retrieving the true surface reflectance of ground objects [36].

After radiation calibration, band fusion, and atmospheric correction, the minimum noise fraction rotation approach concentrated the spectral information of ground objects on the main wavebands. Endmembers were continuously optimized to obtain different land surface types of pure pixels. In this process, we also used 0.5 resolution satellite images to obtain different interpretation samples from some sample areas to assist in density decomposition. Finally, the least squares mixed pixel decomposition model was applied to obtain the density maps of different surface types (i.e., high and low albedo objects, green land space, and soil), accompanied by the corresponding density values of 0.01%-100.00%, respectively. The least squares mixed pixel decomposition model can effectively perform linear decomposition of different land use types, with the advantage that the DN values of abundance maps for each end element within each pixel ranged from 0 to 1. Principle of the model was below.

$$\mathrm{R}_{i\lambda} = \sum_{k=1}^{n} f_{ki} C_{k\lambda} + \varepsilon_{i\lambda} \quad (1)$$

Where $\mathrm{R}_{i\lambda}$ was for the albedo in the i-th pixel from band λ, f_{ki}; was the proportion of the area occupied by k components in the i-th pixel, $\mathrm{C}_{k\lambda}$ was the albedo in the k components from band λ, $\varepsilon_{i\lambda}$ was the residual value.

2.4 Classification of green land type

The green classification was often used to analyze the distribution and diversity of green landscapes, which are important reference landscape indicators for human settlements. Based on the different surface density data that obtained in section 2.3, we used a combination of supervised classification and unsupervised classification to elaborate the urban interior land classification map, thereby extracting the spatial distribution characteristics of green land coverage. The improved normalized water body index was first input into the decision tree classification, with the value over 0 to obtain water coverage. Then, high and low albedo objects density are used to generate impermeable surface areas, green land space density and NDVI were used to obtain vegetation coverage areas, and soil density is used to obtain soil cover. After that, there were still some small areas that cannot be classified by remote sense spectrum.

Preprints (www.preprints.org) | NOT PEER-REVIEWED | Posted: 17 April 2023 doi:10.20944/preprints202304.0424.v1

Unsupervised classification divided these small mixed pixel distribution areas into 200 categories, and manual interpretation identified which land cover type of each classification belonged to. Then, the green land space in urban areas was composed of green coverage from decision trees and small patches of green space unsupervised classification.

2.5 Retrieval of land-surface thermal properties

Land surface radiation energy brings the direct feelings of cold and heat to residents, thereby triggering whether residents are comfortable or not. The spatial scale land surface energy distribution map can be displayed through remote sensing algorithms and actual measurements. To surface energy distribution, the spatial of surface temperature should first be presented [31]. Land surface temperature retrieval model was used to produce spatiotemporal differences in temperature patterns mainly based on the thermal infrared band of Landsat images and the related parameters. The main principles of the model are below. Meanwhile, the air temperature was obtained from a linear equation model of land surface temperature.

$$T_s = A_0 + A_1 T_{10} - A_2 T_{11} \quad (2)$$

$$A_2 = D_{10}/(D_{11}C_{10} - D_{10}C_{11}) + [D_{10}(1 - C_{11} - D_{11})/(D_{11}C_{10} - D_{10}C_{11})]/b_{11} \quad (3)$$

$$A_1 = 1 + D_{10}/(D_{11}C_{10} - D_{10}C_{11}) + [D_{11}(1 - C_{10}D_{10})]/(D_{11}C_{10} - D_{10}C_{11})]b_{11} \quad (4)$$

$$A_0 = [D_{11}(1 - C_{10} - D_{10})/(D_{11}C_{10} - D_{10}C_{11})]\alpha_{10} - [D_{10}(1 - C_{11} - D_{11})/(D_{11}C_{10} - D_{10}C_{11})]\alpha_{11} \quad (5)$$

$$C_i = \varepsilon_i \tau_i(\theta) \quad (6)$$

$$D_i = [1 - \tau_i(\theta)][1 + (1 - \varepsilon_i)\tau_i(\theta)] \quad (7)$$

Where, in the equation 2, T_s was the temperature from land surface, T_{10} and T_{11} was the brightness temperature from Landsat images , A_0 , A_1 and A_2 were the a transition parameter that can be calculated from equations 3-7. And for equations 3-7, τ_i and ε_i represented the surface emissivity and atmospheric transmittance, separately. More parameter explanations were provided in the this study [37].

Then, the surface radiation energy balance model was used to obtain variously spatialized thermal comfort indicators. In this study, sensible heat flux was used to identify heat generation regions so as to explore its impact on residents; and latent heat flux for exploring the suitable region for residents' leisure and available flux for evaluating the total energy that residents obtained in the study area.

$$R_n = (1 - \alpha)R_{sd} + R_{ld} - R_{lu} \quad (8)$$

$$R_n = S + L + Gsoil \quad (9)$$

$$S = SAFR(R_n - Gsoil) \quad (10)$$

$$L = LAFR(R_n - Gsoil) \quad (11)$$

$$Gsoil = (T_s - 273.15)/\alpha(0.0038\alpha + 0.0074\alpha^2)(1 - 0.98NDVI^4)R_n \quad (12)$$

$$AF = S + L \quad (13)$$

Where, in equation 8, R_{sd} , R_{ld} , and R_{lu} represented the indicators of shortwave radiation, downwelling longwave radiation and upwelling longwave radiation, which can be obtained from Ts and corresponding parameters. In equation 9, S, L, and Gsoil was sensible heat flux, latent heat flux, and soil heat flux. These indicators were obtained from equations 10-12, SAFR and LARF were the proportional parameters that were calculated from by pixel component arranging and component algorithm model ([38]). In equation 13, AF was available flux.

Preprints (www.preprints.org) | NOT PEER-REVIEWED | Posted: 17 April 2023 doi:10.20944/preprints202304.0424.v1

3. Results

3.1. Analysis of temporal and spatial characteristics in green land in the whole study area from 2000-2022

3.1.1. Analysis of temporal characteristics of green land change in the whole areas from 2000-2022

In 2000, the total green area was 4670.96 km², accounting for 87.90% of the whole study area. Among them, the coverage areas of cultivated land, forest land, and grassland were 3666.43 km², 653.28 km², and 351.25 km², accounting for 69.00%, 12.29%, and 6.61%, respectively. It can be seen that the green land was mainly composed of cultivated land.

From 2000-2022, the area covered by green land decreased by 474.05 km², resulting in a decrease of 9.17% in its share of the entire study area. From different sub-level type perspectives, the area of cultivated land, forest land and grassland also decreased by 229.16 km², 81.81 km² and 163.08 km². Correspondingly, the proportion of these three types decreased by 4.52%, 1.57% and 3.08%, respectively. This indicates that during the urban development process, the total amount of green land decreased, and different sub-level types of green land also decreased in the whole study area.

By 2022, the total area covered by green land was 4196.91 km², accounting for 78.73% of the whole study area. Meanwhile, the coverage areas of cultivated land, forest land, and grassland were 3437.28 km², 571.46 km², and 188.17 km², respectively. The proportions of these three types were 64.48%, 10.72%, and 3.53%. Data displayed that the pattern of green land constantly changed from 2000-2022.

Table 1 Statistics of green land area and non-green land area from 2000-2022

Classification	**Land types**	**2000 (km²)**	**2005(km²)**	**2010(km²)**
Green land	Cultivated land	3666.43	3617.08	3507.75
	Forest land	653.28	652.28	571.76
	Grassland	351.25	349.52	189.11
Non-green land	Water body	156	165.40	211.60
	Construction land	477.84	522.37	823.18
	Unused land	8.93	8.92	10.33
Classification	Land types	2016(km²)	2022 (km²)	2000-2022 change (km²)
Green land	Cultivated land	3483.55	3437.28	-229.16
	Forest land	571.65	571.46	-81.81
	Grassland	189.00	188.17	-163.08
Non-green land	Water body	212.47	212.29	56.29
	Construction land	846.65	909.1	431.26
	Unused land	10.33	12.42	3.49

3.1.2. Analysis of spatial characteristics of green land change from 2000-2022

For the sub-green land, in the initial year, the spatial feature of cultivated land was widely distributed in the study area, with centralized and scattered patterns coexisting. The forest land was mainly distributed in the middle and north-east regions, along with the form of long strips from northeast to southwest. Grassland was scattered in small clusters. This indicates that different types of green land displayed the differentiated spatial distribution pattern.

By 2022, the loss area covered by green land mainly occurred in the gray legend area in the southeast, which was close to the sea, possibly due to the expansion of construction land and the newly established ports and docks. At the same time, in the northeast and north regions, there was also a certain degree of spatial loss in the coverage of green land. Among them, for the different sub-level types, it can be seen that in the northwest region, the spatial coverage of forest land and grassland has shrunk, in contrast, the pattern of cultivated land has expanded to a certain extent,

Preprints (www.preprints.org) | NOT PEER-REVIEWED | Posted: 17 April 2023 doi:10.20944/preprints202304.0424.v1

indicating that the mutual transformation characteristics of different cover types happened within the different green land regions. The interlaced zone of cultivated land, forest land, and grassland was accompanied by intense internal conversion of different green land.

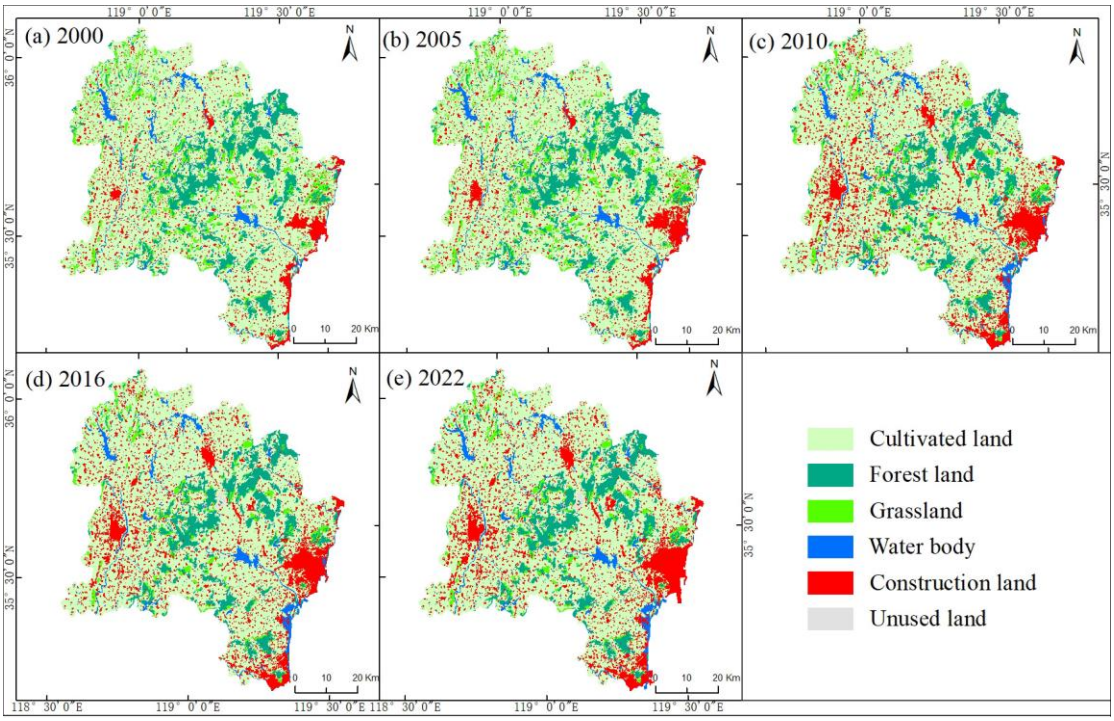

Figure 2 Spatial characteristics of green land and non-green land space in Rizhao region from 2000-2022

3.1.3. Deeply analysis of the temporal and spatial characteristics of green land loss from 2000-2022

Between 2000 and 2022, the green coverage area in the whole study area lost 474.05 km², resulting in a decrease of 9.17% in the proportion, due to the increase in the area of non-green land system. For non-green land system, the area of water, construction land, and other lands in 2000 was 156.00 km², 477.84 km², and 8.93 km², respectively. By 2022, the area of these three non-green land types was 212.29 km², 909.10 km², and 12.42 km². The data indicated that the proportion of these three non-green lands increased by 1.05%, 8.06%, and 0.06% between 2000 and 2022, respectively. Therefore, construction land was the main increment (+8.06%), while the proportion of green land loss in the whole study area between 2000-2022 was 9.17%. The data indicated that the expansion of construction land has brought about the loss of green land, with 87.90% of the loss of green land converted to construction land.

Further, for the spatial pattern of construction land (i.e., urban, rural, and other construction lands), the picture displayed that the red land category (i.e., urban land) was characterized by extending from the center to the surrounding areas in the southeast, middle east, and north central regions of the study area. In its expanded region, the detailed types of green land lost included paddy field, upland crops, forest land, shrub land, sparse forest land, other forest land, high, medium and low coverage grassland, etc. Meanwhile, we found that pink patches (i.e., rural settlements and other construction lands) also have different degrees of expansion characteristics.

Preprints (www.preprints.org) | NOT PEER-REVIEWED | Posted: 17 April 2023 doi:10.20944/preprints202304.0424.v1

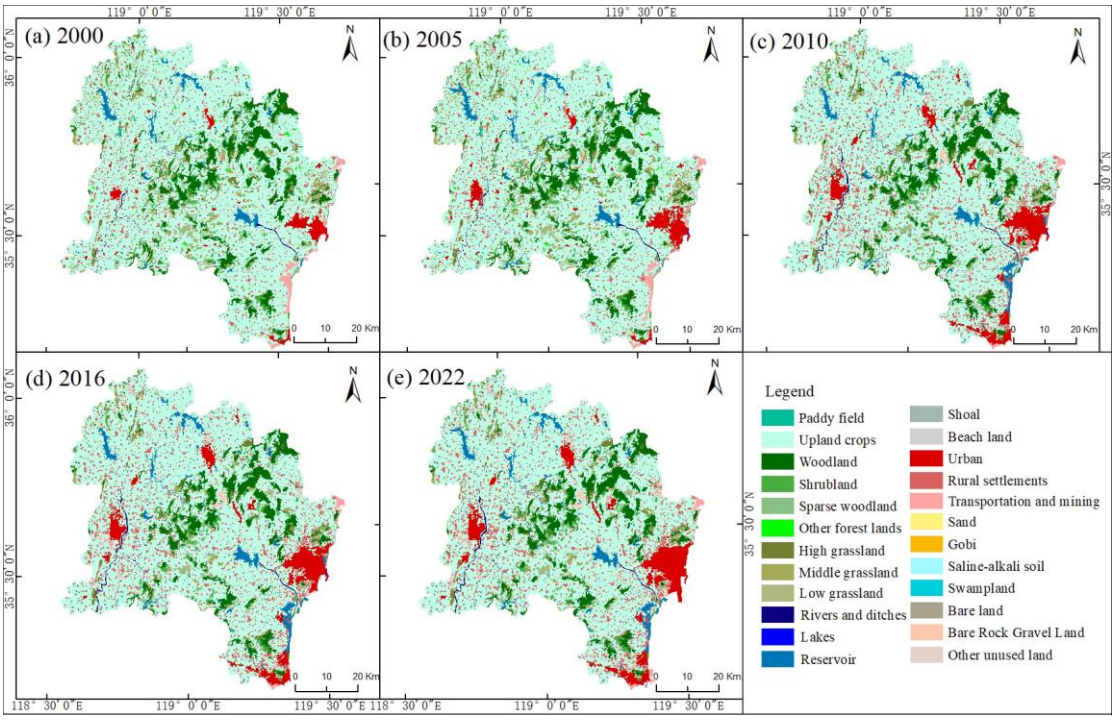

Figure 3 Spatial characteristics of sub-green land and sub-non-green land space in Rizhao region from 2000-2022

3.2. Analysis of spatiotemporal patterns of green land with different urbanization stages from 2000-2022

3.2.1. Analysis of greening rate change at different urbanization stages from 2000-2022

In 2000, China's urbanization process was at an initial stage, and the total built-up region in our study area covered an area of 52.35 km^2, of which the green land covered an area of 13.27 km^2, along with the urban greening rate of 25.34%. For its space distribution, green land space tended to be distributed intensively at the edge of the built-up area, while within the built-up area, it is mainly distributed sporadically.

In 2022, China's urbanization process was already in a rapid development stage, and the urban scope of our research area has also experienced a dramatic expansion, with an increment of 78.54 km^2, an urban expansion rate of 150.03%; And the coverage area of built-up area reached to 130.89 km^2 in 2022. In the process of urban development, green land coverage also showed an increasing trend, with the total increment of 42.98 km^2 from 2000-2022. This indicated that the increase in green land area was as high as 323.94% during the studied period, which far exceeded the growth rate of urbanization at the same time. By 2022, the urban greening rate of the research area reached to 42.97%, and the spatial distribution of green land space presented more aggregation states.

Preprints (www.preprints.org) | NOT PEER-REVIEWED | Posted: 17 April 2023 doi:10.20944/preprints202304.0424.v1

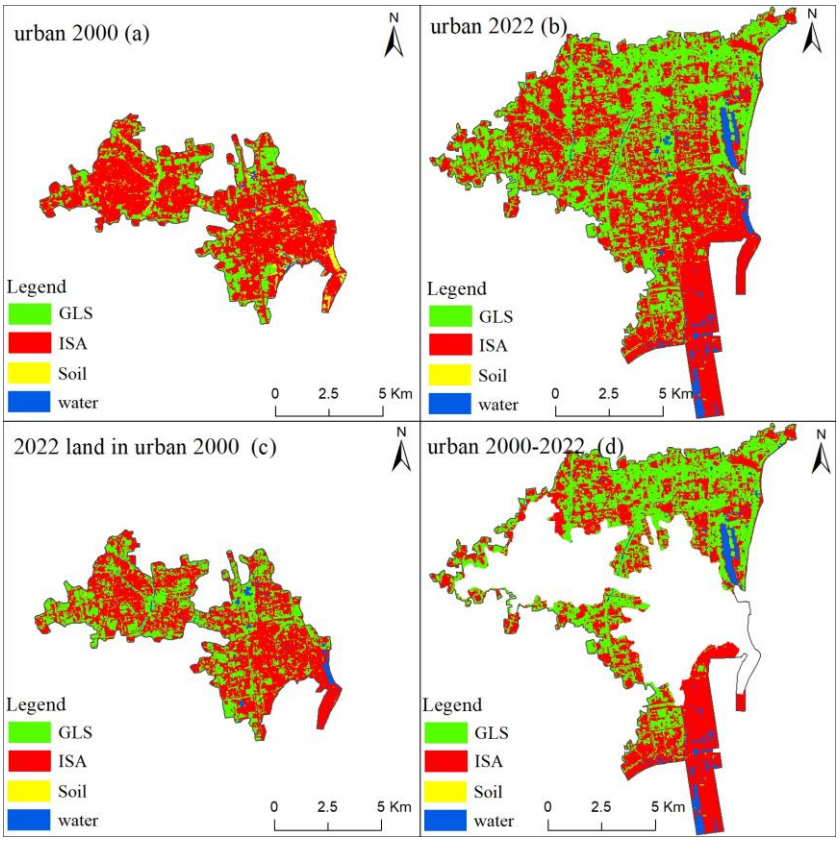

Figure 4 Spatial distribution of green land and non-green land coverage in urban 2000, urban 2000-2022, and urban 2000-2022. Abbreviation: GLS: green land space, ISA: impervious surface area.

3.2.2. Analysis of greening rate change at different urbanization stages from 2000-2022

Here, we analyzed the different greening levels in the old and new urban areas to reflect the important role of green land space for the human settlements. For the old urban regions (i.e., the built-up area boundary in 2000), a fixed built-up area boundary scenario, the total area of green land space was 19.78 km^2 in the year of 2022, with an increase of 6.51 km^2 compared to that of 2000 (i.e., 13.27 km^2). With the boundary of the built-up area unchanged condition, the increase of green land space in old urban areas means the improvement of green land space service functions for the dwellers such as, more places to rest in summer, more beautiful green landscape, and more suitable green space temperature regulation.

Then, we compared the greening level in different built-up area scenarios (i.e., the old and new built-up areas) at the fixed year (i.e., the year of 2022). Here, the new built-up area was region of urban expansion from 2000 to 2022. In the year of 2022, total area of greening land in the new built-up area was 36.47 km^2. Correspondingly, the greening rate of the new built-up area was up to 46.43%, nearly half of the proportion. Meanwhile, the greening rate of the old built-up area was 37.78%. The data indicated that the greening rate of the new urban area was higher 9.96% than that of the old urban area in 2022. Overall, we found that the order of greening level from high to low was new built-up area in 2022, old built-up area in 2022 and old built-up area in 2000.

Preprints (www.preprints.org) | NOT PEER-REVIEWED | Posted: 17 April 2023 doi:10.20944/preprints202304.0424.v1

Table 2 Statistics on the proportion of green land space in different urbanization regions

Urbanization regions	Area (km²)	Proportion (%)
Green land in urban 2000	13.27	25.34
Green land in urban 2005	27.12	32.14
Green land in urban 2010	44.15	38.98
Green land in urban 2016	48.40	40.52
Green land in urban 2022	56.25	42.97
2022 green land in urban 2000	19.78	37.78
Green land in urban 2000-2022	36.47	46.43

3.3. Effects of different thermal factors on the comfort of urban human settlements

3.3.1 Analysis of the characteristics of green land density in urban regions

To further display the distribution of green land space in urban areas, the green land density map was produced, with values in each grid pixel between 0% and 100%. The advantage of this data was that it can accurately depict the proportion of green space per pixel. It can be seen from the figure that the maximum green land density per pixel in the entire urban area can reach 100%. Through calculation, the average green land density in the entire area was 43.35%. The density of green land space coverage was generally high on both sides of the roads and the concentrated park areas, where green land was planted well, bringing comfort to residents. The low value areas of green land density were mainly concentrated in the southeast region that was the place of port. The surface was mainly composed of roads, squares, and port construction facilities, where the greening design was relatively lower and these areas were also the places where residents rarely visited.

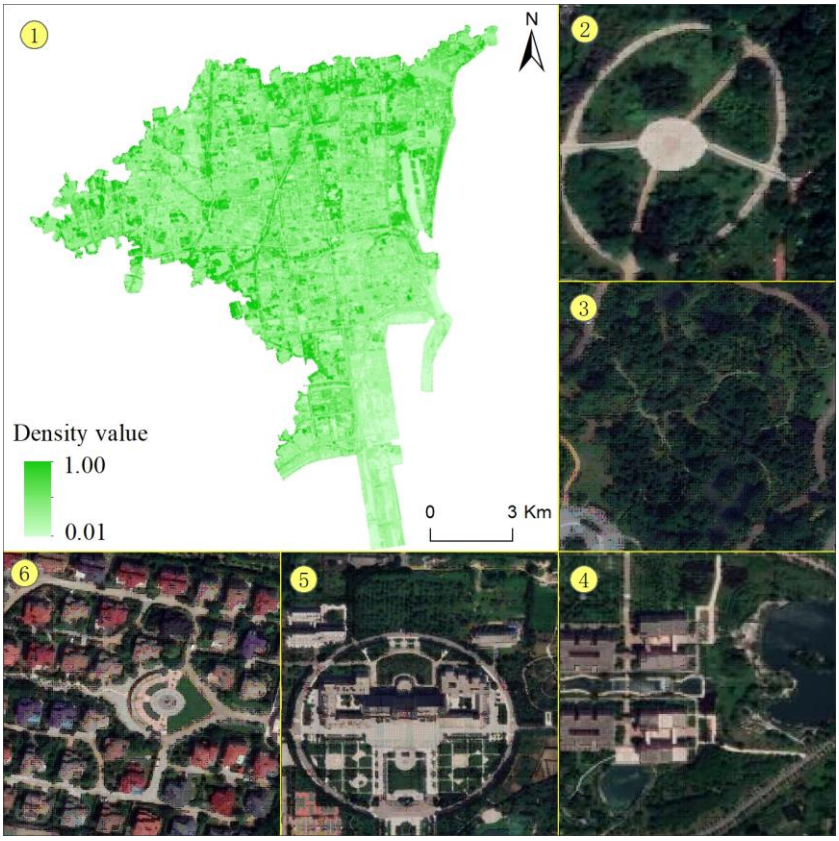

Figure 5 Spatial distribution of green space density. Notes: Labels for circle 2, 3, 4, 5 and 6 represented the regions of coastal green spaces, parks, recreational space, office green space, and residential green space, respectively.

 doi:10.20944/preprints202304.0424.v1

3.3.2 Analysis of spatial distribution characteristics of thermal comfort factors affecting residents

From the perspective of residents' actual perceived energy, we selected sensible heat flux, latent heat flux, total available flux and others as thermal comfort factors. Especially, sensible heat flux was used to understand the spatial pattern of heat generation within urban region, combining with the distribution of urban residents and corresponding measures, to weaken the overheated region. In contrast, latent heat flux primarily identified the areas of supercooling. The total available flux varied in different regions and latitudes, so it was also an important indicator in analyzing the impact of flux on residents' thermal comfort.

For sensible heat flux, the distribution diagram of sensible heat flux in the urban area can be seen from the legend that the lowest value of the entire urban area was 0, indicating that some areas within the urban area did not display any sensible heat energy, that is, there was no heat source. The highest value was 457.83 W/m^2, indicating that in local areas, the heat emission was still very high. We found that the sensible heat flux in urban areas presented a significant gradient feature, with high value areas mainly concentrated in the western region, which was also mainly the old urban area. The construction of houses, roads, and squares was relatively dense.

For latent heat flux, the highest latent heat flux in the entire urban area was 645.09 W/m^2, mainly distributed in the east of the urban area, close to the seaside, which was also the location of the Shanhaitian National Tourism Resort, indicating that this area generally had a higher latent heat flux than other areas, providing residents with a more cool and comfortable environmental experience and feeling. At the same time, it was also seen that the highest values generally occured in water bodies, indicating that whether it was concentrated and contiguous rivers, ponds, fountains, etc., can provide a comfortable water environment for residents.

For total available flux, it can be seen from the figure that the lowest available flux in the urban area was 254.07 W/m^2, and the data indicated that there was no area with an energy of 0,. At the same time, we further found that the maximum energy value was 659.42 W/m^2, which was the maximum value of the superposition of latent heat flux and sensible heat flux, and was also higher than the maximum value of a single latent heat flux or a single sensible heat flux. The change in this value means a change in energy, which had an impact on residents' comfort perception. Through calculation, the average value of available flux was 492.75 W/m^2, which also first represented the average impact of the total energy available per unit area of the study area on the thermal comfort of residents' homes. Also, spatial distribution maps of other thermal comfort factors such as soil heat flux, albedo, and net radiation were calculated and provided in figure 6, respectively.

Preprints (www.preprints.org) | NOT PEER-REVIEWED | Posted: 17 April 2023 doi:10.20944/preprints202304.0424.v1

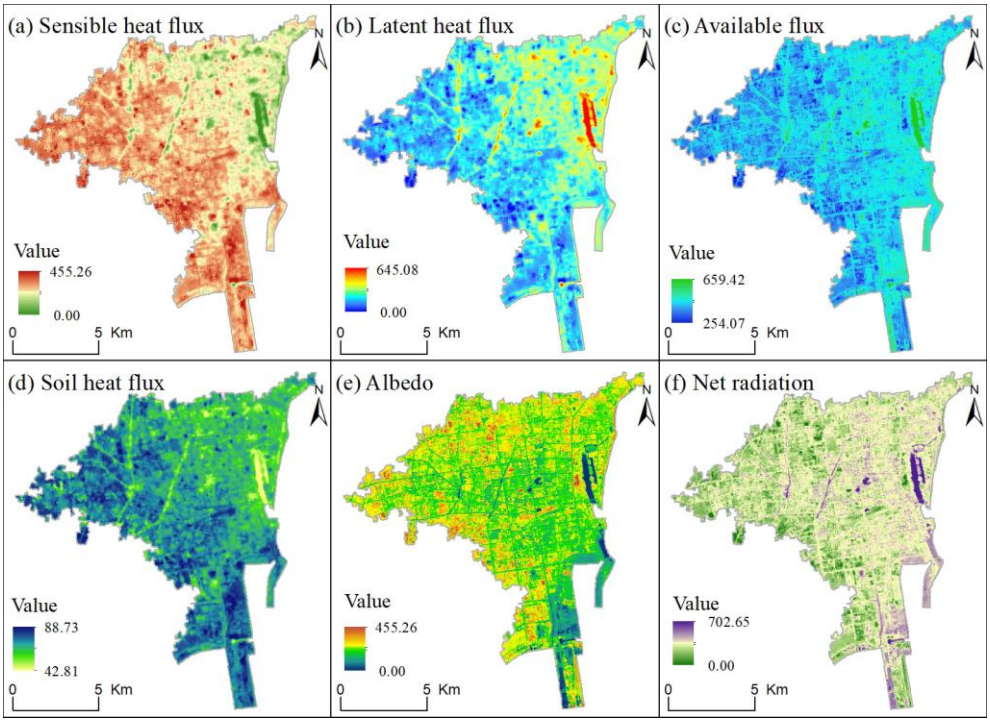

Figure 6 Land-surface thermal property of sensible heat flux, latent heat flux, available flux, soil heat flux, albedo and net radiation.

3.4. Analysis on the cooling effect of green land and its impact on urban residential environments

3.4.1 Characterizing the cooling temperature effect of different green land densities in this coastal region

Using the green land density data as the basic data source and combining with the spatial distribution data of land surface temperature, the cooling temperature effect of green land density was investigated. The green land density data with values ranging from 0.01% to 100% was divided into three levels, namely, the low, medium, and high-density green land, with corresponding values of 0.01% to 33.33%, 33.33% to 66.66%, and 66.66% to 100.00%, respectively. By superposing these three density areas to the land surface temperature, the lowered cooling temperature values in the middle and high green land density region were 1.05 ℃ and 2.12 ℃ using the temperature value in the low density land green region as the reference. Data indicated that in coastal area the land temperature reduction effect of the green land became stronger as the green area coverage increased, even over 2 ℃ compared to the low green land density region.

3.4.2 Analysis of spatial distribution characteristics of cold and hot uncomfortable areas in residential environment region

Based on the analysis of cooling temperature effect of green land densities, the spatiotemporal pattern of air temperature was further explored, due to the air temperature was often a direct and key factor to impact of thermal comfort on dwellers. It can be seen from the figure that the minimum air temperature in urban areas was 15.85 ℃, mainly distributed in areas where rivers were concentrated, and the maximum air temperature was 36.64 ℃, mainly concentrated in the polymerization effect area of buildings. Therefore, the variation range of air temperature was 18.79 ℃, and the average air temperature is 25.86 ℃. According to relevant references, we set the air temperature above 30 ℃ as a thermal discomfort zone (Figure 7 upper left figure, red legend), and the air temperature region 18 ℃ as a cold discomfort zone (Figure 7, upper right corner, blue legend) in the summer season. The spatial distribution of uncomfortable areas was below. The proportions of hot and cold uncomfortable regions were 4.22% and 5.15%, respectively.

Preprints (www.preprints.org) | NOT PEER-REVIEWED | Posted: 17 April 2023 doi:10.20944/preprints202304.0424.v1

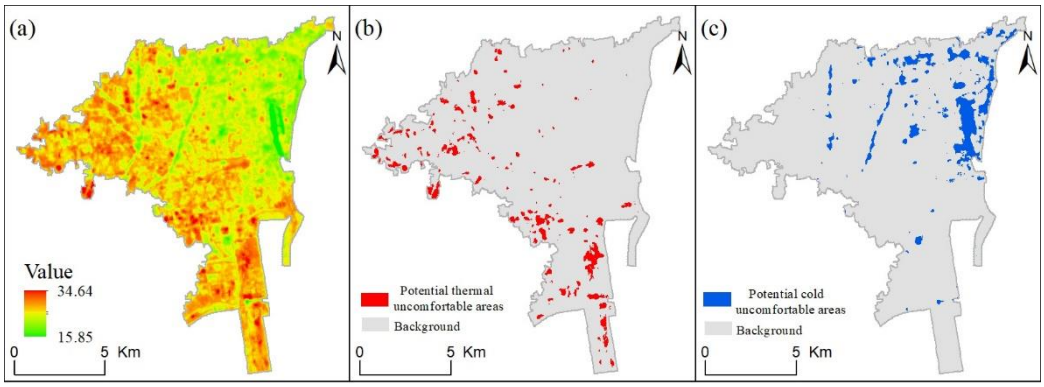

Figure 7 (a) Air temperature distribution and corresponding (b) comfort and (c) discomfort regions

4. Discussion

4.1 A highly greening and livable region in the central coast of China

In response to explore the spatiotemporal heterogeneity of green land space, a typical region in the central coast of China from 2000-2022 was investigated in this study. We detected a high coverage of green land space in the study area, and there were significant differences in urban greening rates among different urbanization regions. In 2000, the greening rate was 25.34% in the built-up area, and raised to 42.97% in 2022, along with the percentage increment of 17.63%. This means that the proportion of green land space in urban development has been significantly increased. The green land space coverage rate in the study area is in the forefront in China [39]. Urban development is paying more and more attention to the role of green land space [39,40], considering the comfort environment function of green land space for the residents such as absorbing carbon dioxide and releasing oxygen, thereby improving urban ecosystem services [41,42].

High vegetation greening rate plays an important role in the comfort of human settlements. Based on the monitoring of this study, the urban greening rate was up to 46.43% in the new urban area (i.e., the urban expansion area from 2000 to 2022). This means that nearly half of the new urban area was covered by green land space. According to our field investigation, in the new built-up area, the green land space includes the centralized and scattered park green space, the community green space, the road shade, the parking lot shade, the three-dimensional configuration of grassland landscape, the green of square, trellis and flower rack, the greening fence regions, greening around the sports ground, and greening roof, etc. High coverage of green space also attracts tourists from other places. The rich and beautiful green space design not only provides local residents a comfortable feeling, but also attracts a large number of foreign tourists to come for sightseeing.

The study area also makes full use of green space and water resources for urban construction from the concept of human settlements and obtained the titles of National Civilized City, National Forest City, National Environmental Protection Key City, and National Ecological Demonstration Zone Construction Pilot City in China. These honors fully affirmed that the green space and ecological environment construction of the research area is at the forefront of China. Meanwhile, Rizhao was also named the "Capital of Water Sports" and "Oriental Sun City" based on Natural environment from water resources and geographical location. Furthermore, Rizhao won the United Nations Habitat Award that was an honor to evaluate the livability of a city. This city has become a green and livable region in China.

4.2 Compare the differentiated green land structures in different climatic regions at home and abroad

The urban green land space under different climatic backgrounds was first compared and analyzed in China. In western China, especially in the arid and semi-arid regions of northwest China [43-45], large areas of green planting are usually carried out in urban areas, in order to combat the arid climate and provide better ecosystem services for residents; and the proportion of green space is always less than 20% in urban regions. In contrast, in eastern China, a humid and semi-humid region [46-48], the proportion of green space within the city is relatively high compared the arid and semi-arid regions, such as the Beijing, the capital city of China, the proportion of green space was nearly 30% to the built up area in the year of 2021. Further, in the coastal regions, the proportion of green space in built-up areas has further increased such as the study area in this paper, the value was up to approximately 43% in the year of 2022. Different climatic backgrounds are one of the important factors affecting the proportion of urban green land space.

The green land space in urban areas in different regions of the world was then investigated. Relevant research indicated that the proportion of urban green land to the corresponding built-up area boundary decreased by 13.93%

Preprints (www.preprints.org) | NOT PEER-REVIEWED | Posted: 17 April 2023 doi:10.20944/preprints202304.0424.v1

and 7.28% in Capital cities of East Asia and South Asia from 2000-2015 [49]. In the meantime, Increases in the proportion of green land to the built-up area happened in the Middle East and Central Asia, along with the incremental values of 12.61% and 15.36%, respectively. As for Europe, the spatial patterns of the cities were basically stable, with relatively small change in green land; And the increase in the proportion of green land was only 1.57%. Therefore, the proportion of green land in built-up areas in different regions varied significantly.

4.3 Possibly positive effects of densely green land space on the comfort of human welfare

Densely green spaces in Rizhao and other regions of the world may have the positive impact on human well-being. Firstly, increasing aerobic exercise and improving the comfort of physical and mental health. Photosynthesis of forest and grassland in high green space may promote the local production of a high concentration of "oxygen bar" environment [50], similarly to a business place for people to breathe oxygen. Residents can rest and walk in such an environment, so that people's cerebral cortex and brain activities are strengthened, which may promote the absorption of oxygen content, accelerate blood circulation, invigorate the spirit, eliminate fatigue, and improve immunity [51,52]. In such an environment, residents feel the beauty of the natural environment. Secondly, improving comfort of leisure and mood [53,54]. According to our survey, the service radius for Rizhao residents to reach parks and centralized green spaces is less than 500 meters. This was similar to the situation in high green areas of developed countries in the Americas and Europe, which was featured by a large population and high coverage of urban green land spaces. The shorter the service radius of park green and centralized green land spaces is more convenient for residents to stroll and relax [55]. Most of their transportation ways to these greening regions are mainly walking or cycling, which is not only green and environmentally friendly, but also has a mood enhancing effect. However, If the service radius of park green spaces and centralized green spaces is large and far [56], like the regions of Africa and other arid regions, people have to use private cars or public transportation to reach greening land regions. This not only generates noise pollution and is prone to traffic congestion, which affects residents' mood, but also makes the exhaust gas from fuel powered vehicles more likely to pollute the environment and generate greenhouse temperature emissions, which is not conducive to the United Nations Sustainable Development Goals (i.e., SDGs [57]) target.

5. Conclusions

To address the shortcomings of current research on spatiotemporal heterogeneity of coastal green land space and its impact on human settlements comfort in the central coast region of China, taking the Rizhao region as the research area, which was known for its coastal ecology, livability and greenery in China and obtained the United Nations habitat award, the paper analyzed spatiotemporal patterns of green land at different urban regions, further explored the effects of different thermal factors on the comfort of urban human settlements and quantified the cooling effect of green land, the main conclusions obtained were as follows:

(1) For the spatiotemporal change pattern of green land, in 2000, the total area of green land was 4670.96 km^2, accounting for 87.90% of the study area. From 2000 to 2022, the green land area decreased by 474.05 km^2, resulting in a decrease of 9.17% in its share of the entire study area; and by 2022, the total area covered by green land was 4196.91 km^2, accounting for 78.73%. For the sub-level types, the green land was mainly composed of cultivated land. The interlaced zone of cultivated land, forest land, and grassland was accompanied by intense internal conversion of different green land.

(2) For the greening levels, a fixed built-up area boundary scenario, the green land proportion in old urban areas was 25.34% in 2000, and by 2022, this proportion increased to 37.78%, the increase of green land space in old urban areas means the improvement of green land service functions for the dwellers. Furthermore, the proportion was up to 46.43% in new urban areas. More attention was paid to the construction of urban green space during urban expansion, which will inevitably bring better visual and comfort experience to residents.

(3) For the characteristics of thermal comfort indicators, we analyzed the variation range of each comfort indicator, such as the latent heat flux (0-457.83 W/m^2), sensible heat flux (0-645.09 W/m^2), and total available energy (254.07-659.42 W/m^2), and further provided the spatial distribution pattern of each indicator in the study area.

(4) For the cold effect on green land space and temperature effect, the lowered cooling temperature values in the middle and high green land density region were 1.05 ℃ and 2.12 ℃ using the temperature value in the low-density land green region as the reference. And the minimum air temperature in urban areas was 15.85 ℃, mainly distributed in areas where rivers were concentrated, and the maximum air temperature was 36.64 ℃, mainly concentrated in the polymerization effect area of buildings. The variation range of air temperature was 18.79 ℃, and the average air temperature is 25.86 ℃. Finally, the spatial distribution pattern of hot and cold uncomfortable areas was also given. This

research results provided the significant reference for the study of green land pattern and the impact on the land-surface thermal property of human settlements in coastal areas of China and worldwide.

Author Contributions: Conceptualization, Tao. Pan and Shanfeng. He; methodology, writing—original draft preparation, Tao. Pan; writing—review and editing, Tao.Pan, Shanfeng He, Zhaoyu Liu, Liming Jiang, Qinglei Zhao, Rafiq hamdi.

Funding: This study is supported by Natural science foundation youth program of Shandong Province (grant no. ZR2021QD134) and the Young Taishan Scholars Program of Shandong Province (grant no. tsqn202103065).

Conflicts of Interest: The authors declare no conflict of interest.

References

1. Bell, S.L.; Phoenix, C.; Lovell, R.; Wheeler, B.W. Seeking everyday wellbeing: The coast as a therapeutic landscape. *Social Science & Medicine* **2015**, *142*, 56-67.
2. Fu, S.; Zhang, X.; Kuang, W.; Guo, C. Characteristics of Changes in Urban Land Use and Efficiency Evaluation in the Qinghai–Tibet Plateau from 1990 to 2020. *Land* **2022**, *11*, 757.
3. He, B.-J.; Wang, J.; Liu, H.; Ulpiani, G. Localized synergies between heat waves and urban heat islands: Implications on human thermal comfort and urban heat management. *Environmental Research* **2021**, *193*, 110584.
4. Zou, Z.; Yan, C.; Yu, L.; Jiang, X.; Ding, J.; Qin, L.; Wang, B.; Qiu, G. Impacts of land use/land cover types on interactions between urban heat island effects and heat waves. *Building and Environment* **2021**, *204*, 108138.
5. García, D.H. Analysis of urban heat island and heat waves using Sentinel-3 images: a study of Andalusian Cities in Spain. *Earth Systems and Environment* **2022**, 1-21.
6. Yin, J.; Fu, P.; Cheshmehzangi, A.; Li, Z.; Dong, J. Investigating the Changes in Urban Green-Space Patterns with Urban Land-Use Changes: A Case Study in Hangzhou, China. *Remote Sensing* **2022**, *14*, 5410.
7. Wu, W.; Yuan, Y.; Huang, C.; Dong, W.; Fu, Z. Urban Green Land Ecological Suitability Assessment Based on GIS in Arid Areas: Beitun City, Xinjiang, as an Example. *Polish Journal of Environmental Studies* **2021**, *30*, 5871-5883.
8. Liu, Y.; Zhou, Y. Reflections on China's food security and land use policy under rapid urbanization. *Land Use Policy* **2021**, *109*, 105699.
9. Tappert, S.; Klöti, T.; Drilling, M. Contested urban green spaces in the compact city: The (re-) negotiation of urban gardening in Swiss cities. *Landscape and urban planning* **2018**, *170*, 69-78.
10. Fan, F.; Lian, H.; Liu, X.; Wang, X. Can environmental regulation promote urban green innovation Efficiency? An empirical study based on Chinese cities. *Journal of Cleaner Production* **2021**, *287*, 125060.
11. Sun, L.-L.; Cui, H.-J.; Ge, Q.-S. Will China achieve its 2060 carbon neutral commitment from the provincial perspective? *Advances in Climate Change Research* **2022**, *13*, 169-178.
12. Shi, X.; Zheng, Y.; Lei, Y.; Xue, W.; Yan, G.; Liu, X.; Cai, B.; Tong, D.; Wang, J. Air quality benefits of achieving carbon neutrality in China. *Science of the Total Environment* **2021**, *795*, 148784.
13. Wang, Y.; Guo, C.-h.; Chen, X.-j.; Jia, L.-q.; Guo, X.-n.; Chen, R.-s.; Zhang, M.-s.; Chen, Z.-y.; Wang, H.-d. Carbon peak and carbon neutrality in China: Goals, implementation path and prospects. *China Geology* **2021**, *4*, 720-746.
14. Guo, A.; Yang, J.; Sun, W.; Xiao, X.; Cecilia, J.X.; Jin, C.; Li, X. Impact of urban morphology and landscape characteristics on spatiotemporal heterogeneity of land surface temperature. *Sustainable Cities and Society* **2020**, *63*, 102443.
15. Yun, J.; Yu, W.; Wang, H. Exploring the Distribution of Gardens in Suzhou City in the Qianlong Period through a Space Syntax Approach. *Land* **2021**, *10*, 659.
16. De Sousa, C.A. The greening of brownfields in American cities. *Journal of Environmental Planning and Management* **2004**, *47*, 579-600.
17. Joyce, K.E.; Belliss, S.E.; Samsonov, S.V.; McNeill, S.J.; Glassey, P.J. A review of the status of satellite remote sensing and image processing techniques for mapping natural hazards and disasters. *Progress in physical geography* **2009**, *33*, 183-207.

18. Behnam, A.; Wickramasinghe, D.C.; Ghaffar, M.A.A.; Vu, T.T.; Tang, Y.H.; Isa, H.B.M. Automated progress monitoring system for linear infrastructure projects using satellite remote sensing. *Automation in construction* **2016**, *68*, 114-127.
19. Amani, M.; Ghorbanian, A.; Ahmadi, S.A.; Kakooei, M.; Moghimi, A.; Mirmazloumi, S.M.; Moghaddam, S.H.A.; Mahdavi, S.; Ghahremanloo, M.; Parsian, S. Google earth engine cloud computing platform for remote sensing big data applications: A comprehensive review. *IEEE Journal of Selected Topics in Applied Earth Observations and Remote Sensing* **2020**, *13*, 5326-5350.
20. Chen, B.; Xu, B.; Zhu, Z.; Yuan, C.; Suen, H.P.; Guo, J.; Xu, N.; Li, W.; Zhao, Y.; Yang, J. Stable classification with limited sample: Transferring a 30-m resolution sample set collected in 2015 to mapping 10-m resolution global land cover in 2017. *Sci. Bull* **2019**, *64*, 370-373.
21. Ning, J.; Liu, J.; Kuang, W.; Xu, X.; Zhang, S.; Yan, C.; Li, R.; Wu, S.; Hu, Y.; Du, G. Spatiotemporal patterns and characteristics of land-use change in China during 2010–2015. *Journal of Geographical Sciences* **2018**, *28*, 547-562.
22. Kuang, W.; Liu, J.; Dong, J.; Chi, W.; Zhang, C. The rapid and massive urban and industrial land expansions in China between 1990 and 2010: A CLUD-based analysis of their trajectories, patterns, and drivers. *Landscape and Urban Planning* **2016**, *145*, 21-33.
23. Zhao, G.; Liu, J.; Kuang, W.; Ouyang, Z.; Xie, Z. Disturbance impacts of land use change on biodiversity conservation priority areas across China: 1990–2010. *Journal of Geographical Sciences* **2015**, *25*, 515-529.
24. Nikolopoulou, M.; Baker, N.; Steemers, K. Thermal comfort in outdoor urban spaces: understanding the human parameter. *Solar energy* **2001**, *70*, 227-235.
25. Błażejczyk, K.; Jendritzky, G.; Bröde, P.; Fiala, D.; Havenith, G.; Epstein, Y.; Psikuta, A.; Kampmann, B. An introduction to the universal thermal climate index (UTCI). *Geographia Polonica* **2013**, *86*, 5-10.
26. Jendritzky, G.; Maarouf, A.; Fiala, D.; Staiger, H. An update on the development of a Universal Thermal Climate Index. In Proceedings of the 15th Conf. biomet. aerobiol. and 16th ICB02, 2002; pp. 129-133.
27. Yaghoobian, N.; Srebric, J. Influence of plant coverage on the total green roof energy balance and building energy consumption. *Energy and Buildings* **2015**, *103*, 1-13.
28. Kuang, W.; Dou, Y. Investigating the patterns and dynamics of urban green space in China's 70 major cities using satellite remote sensing. *Remote Sensing* **2020**, *12*, 1929.
29. Young, R.F. Managing municipal green space for ecosystem services. *Urban forestry & urban greening* **2010**, *9*, 313-321.
30. Lamchin, M.; Lee, J.-Y.; Lee, W.-K.; Lee, E.J.; Kim, M.; Lim, C.-H.; Choi, H.-A.; Kim, S.-R. Assessment of land cover change and desertification using remote sensing technology in a local region of Mongolia. *Advances in Space Research* **2016**, *57*, 64-77.
31. Yu, X.; Guo, X.; Wu, Z. Land surface temperature retrieval from Landsat 8 TIRS—Comparison between radiative transfer equation-based method, split window algorithm and single channel method. *Remote sensing* **2014**, *6*, 9829-9852.
32. Chakraborty, S.D.; Kant, Y.; Mitra, D. Assessment of land surface temperature and heat fluxes over Delhi using remote sensing data. *Journal of environmental management* **2015**, *148*, 143-152.
33. Burakowski, E.; Tawfik, A.; Ouimette, A.; Lepine, L.; Novick, K.; Ollinger, S.; Zarzycki, C.; Bonan, G. The role of surface roughness, albedo, and Bowen ratio on ecosystem energy balance in the Eastern United States. *Agricultural and Forest Meteorology* **2018**, *249*, 367-376.
34. Townshend, J.R.; Justice, C. Analysis of the dynamics of African vegetation using the normalized difference vegetation index. *International journal of remote sensing* **1986**, *7*, 1435-1445.
35. Wyatt, C. *Radiometric calibration: theory and methods*; Elsevier: 2012.
36. Cooley, T.; Anderson, G.P.; Felde, G.W.; Hoke, M.L.; Ratkowski, A.J.; Chetwynd, J.H.; Gardner, J.A.; Adler-Golden, S.M.; Matthew, M.W.; Berk, A. FLAASH, a MODTRAN4-based atmospheric correction algorithm, its application and validation. In Proceedings of the IEEE international geoscience and remote sensing symposium, 2002; pp. 1414-1418.
37. Rozenstein, O.; Qin, Z.; Derimian, Y.; Karnieli, A. Derivation of land surface temperature for Landsat-8 TIRS using a split window algorithm. *Sensors* **2014**, *14*, 5768-5780.

38. Liu, K.; Su, H.; Wang, W.; Yang, L.; Liang, H.; Li, X. Comparative assessment of Two Source of Landsat TM vegetative fraction coverage for modeling urban latent heat fluxes. In Proceedings of the 2016 IEEE International Geoscience and Remote Sensing Symposium (IGARSS), 2016; pp. 6762-6765.
39. Piao, S.; Yin, G.; Tan, J.; Cheng, L.; Huang, M.; Li, Y.; Liu, R.; Mao, J.; Myneni, R.B.; Peng, S. Detection and attribution of vegetation greening trend in China over the last 30 years. *Global change biology* **2015**, *21*, 1601-1609.
40. Yao, L.; Li, T.; Xu, M.; Xu, Y. How the landscape features of urban green space impact seasonal land surface temperatures at a city-block-scale: An urban heat island study in Beijing, China. *Urban Forestry & Urban Greening* **2020**, *52*, 126704.
41. Shi, Y.; Shi, D.; Zhou, L.; Fang, R. Identification of ecosystem services supply and demand areas and simulation of ecosystem service flows in Shanghai. *Ecological Indicators* **2020**, *115*, 106418.
42. Wang, B.; Gao, P.; Niu, X.; Sun, J. Policy-driven China's Grain to Green Program: Implications for ecosystem services. *Ecosystem services* **2017**, *27*, 38-47.
43. Cao, S.; Chen, L.; Yu, X. Impact of China's Grain for Green Project on the landscape of vulnerable arid and semi-arid agricultural regions: A case study in northern Shaanxi Province. *Journal of Applied Ecology* **2009**, *46*, 536-543.
44. An, W.; Li, Z.; Wang, S.; Wu, X.; Lu, Y.; Liu, G.; Fu, B. Exploring the effects of the "Grain for Green" program on the differences in soil water in the semi-arid Loess Plateau of China. *Ecological Engineering* **2017**, *107*, 144-151.
45. Pan, T.; Lu, D.; Zhang, C.; Chen, X.; Shao, H.; Kuang, W.; Chi, W.; Liu, Z.; Du, G.; Cao, L. Urban land-cover dynamics in arid China based on high-resolution urban land mapping products. *Remote Sensing* **2017**, *9*, 730.
46. Yu, L.; Liu, Y.; Liu, T.; Yan, F. Impact of recent vegetation greening on temperature and precipitation over China. *Agricultural and Forest Meteorology* **2020**, *295*, 108197.
47. Li, Y.; Piao, S.; Chen, A.; Ciais, P.; Li, L.Z. Local and teleconnected temperature effects of afforestation and vegetation greening in China. *National Science Review* **2020**, *7*, 897-912.
48. Guo, R.; Bai, Y. Simulation of an urban-rural spatial structure on the basis of green infrastructure assessment: the case of Harbin, China. *Land* **2019**, *8*, 196.
49. Pan, T.; Kuang, W.; Hamdi, R.; Zhang, C.; Zhang, S.; Li, Z.; Chen, X. City-level comparison of urban land-cover configurations from 2000–2015 across 65 countries within the Global Belt and Road. *Remote Sensing* **2019**, *11*, 1515.
50. Boldina, A.; Chung, H.C.; Santos, A.M.C.; Steemers, K. Active urbanism: heart rate and oxygen consumption comparison when walking on imitation steppingstones versus a plain surface. *Cities & Health* **2022**, 1-18.
51. Hall, C.; Knuth, M. An update of the literature supporting the well-being benefits of plants: A review of the emotional and mental health benefits of plants. *Journal of Environmental Horticulture* **2019**, *37*, 30-38.
52. Park, S.; Kim, E.; Kim, G.; Kim, S.; Choi, Y.; Paek, D. What activities in forests are beneficial for human health? A systematic review. *International Journal of Environmental Research and Public Health* **2022**, *19*, 2692.
53. Piva, G.; Caruso, L.; Gómez, A.C.; Calzolari, M.; Visintin, E.P.; Davoli, P.; Manfredini, F.; Storari, A.; Spinozzi, P.; Lamberti, N. Effects of forest walking on physical and mental health in elderly populations: a systematic review. *Reviews on Environmental Health* **2022**.
54. Peters, K. Being together in urban parks: Connecting public space, leisure, and diversity. *Leisure Sciences* **2010**, *32*, 418-433.
55. Liu, H.; Li, F.; Li, J.; Zhang, Y. The relationships between urban parks, residents' physical activity, and mental health benefits: A case study from Beijing, China. *Journal of environmental management* **2017**, *190*, 223-230.
56. Zhai, Y.; Wu, H.; Fan, H.; Wang, D. Using mobile signaling data to exam urban park service radius in Shanghai: methods and limitations. *Computers, Environment and Urban Systems* **2018**, *71*, 27-40.
57. Fritz, S.; See, L.; Carlson, T.; Haklay, M.; Oliver, J.L.; Fraisl, D.; Mondardini, R.; Brocklehurst, M.; Shanley, L.A.; Schade, S. Citizen science and the United Nations sustainable development goals. *Nature Sustainability* **2019**, *2*, 922-930.